

CHANDRA OBSERVATION OF NGC 6822

ALLYN F. TENNANT

NASA Marshall Space Flight Center, VP 62, Huntsville, AL 35812; allyn.tennant@msfc.nasa.gov

Received 2006 March 1; accepted 2006 June 6

ABSTRACT

Chandra observed the nearby dwarf galaxy NGC 6822. There are 70 sources in the *Chandra* field, two of which are fairly extended and likely background clusters of galaxies. A third source was resolved by *Chandra* that has the same size and position as a known supernova remnant. The suspected variability detected from this source in previous missions is shown to be in error. The majority of the remaining 67 sources are consistent with background sources. Of the 61 sources detected above a completeness limit of 10 events, we estimate that $9 \pm 4 \pm 8$ are associated with the galaxy, including both systematic and statistical errors. We compare the X-ray positions of all sources with various catalogs and *Hubble Space Telescope* data and offer tentative identifications for several. Based on the mass and star formation rate of NGC 6822, we expect only about 10 sources, mostly high-mass systems.

Key words: galaxies: individual (NGC 6822) — methods: data analysis — X-rays: galaxies

1. INTRODUCTION

The high spatial resolution of *Chandra* (see Weisskopf et al. 2002 and references therein) has greatly facilitated the study of the X-ray-source population of nearby galaxies. Studies of M81 (Tennant et al. 2001; Swartz et al. 2003), for example, show that a single *Chandra* observation can reveal hundreds of discrete X-ray sources with luminosities above 10^{36} ergs s⁻¹. The majority of these sources are expected to be luminous accreting X-ray binaries (both high-mass X-ray binaries [HMXBs] and low-mass X-ray binaries [LMXBs]). Identification of most X-ray sources in the Milky Way requires precise positions, as well as detailed optical follow-up work, because of source confusion at optical and near-IR wavelengths. Since M81 is 360 times further away than the Galactic center, we would require ~ 360 times the spatial resolution with 10^4 greater sensitivity to achieve similar precision.

One alternative is to study Local Group galaxies. Collectively, the Local Group displays most of the variety of X-ray emission characteristics and large-scale morphological structures seen in the more distant resolvable galaxies. Studies of X-ray sources in Local Group galaxies have the advantage that the distance to the sources is more accurately known and, in the case of face-on galaxies, the observations are less affected by intervening material compared to studies of sources in the plane of the Milky Way.

The difficulty with X-ray studies of the Local Group members is that nearby galaxies occupy a relatively large portion of the sky. Except for dwarf galaxies, observations of Local Group galaxies require multiple pointings to image the entire galaxy. The large angular size of Local Group galaxies introduces an additional complication, in that a larger field encompasses a larger number of unrelated background objects.

The IB(s)m Local Group galaxy NGC 6822 is one of the nearest galaxies to the Milky Way at a distance of only 500 kpc. Although the Large and Small Magellanic Clouds are closer, they are far larger than the *Chandra* detectors. NGC 6822 is close to an ideal *Chandra* target in that the galaxy fits nicely on the ACIS-I array. A single 30 ks *Chandra* exposure can cover the entire galaxy down to a luminosity limit of 10^{35} ergs s⁻¹.

Einstein detected two sources in the NGC 6822 field (Markert & Donahue 1985). These sources correspond to *Chandra* sources s34 and s64. They suggested that s34 was a supernova (SN) rem-

nant, a result now totally confirmed by *Chandra*. The *ROSAT* observation of NGC 6822 was analyzed by Eskridge & White (1997), and again the SN remnant was detected.

In this paper we use a distance of 500 ± 20 kpc from Gallart et al. (1996), although recent Cepheid work by Pietrzyński et al. (2004) gives a slightly smaller distance of 470 ± 20 kpc. The Galactic column is about 1×10^{21} cm⁻² (Dickey & Lockman 1990), although the column within NGC 6822 can be several times larger.

2. OBSERVATIONS

NGC 6822 was observed for 28.1 ks by *Chandra* on 2002 November 4. The I-array CCDs plus S2 were operated in the normal 3.14 s time exposure mode. The S2 chip was mostly used as a background monitor, and since it was far off-axis did not yield any other useful information about NGC 6822.

2.1. Data Reduction

We started with the level 1 *Chandra* data as provided by the *Chandra* X-ray Center. The first step was to run the CIAO¹ routine `acis_process_events` to remove the pixel randomization and apply the current charge transfer inefficiency correction. The data file was then filtered to apply the good time interval filter and retain *ASCA* grades 0, 2, 3, 4, and 6. Hot pixels were searched for, but none were found in these data.

We next column-cleaned the data by looking at the data for each CCD in chip coordinates. This is a variation of a method originally used at Pennsylvania State University.² If a column has significantly more counts than its nearest neighbors, then events with the most common grade were removed from that column. Grades were removed until the count rate in that column was consistent with its nearest neighbors. Since the spectral distribution of events has an impact on the grade distribution, this does slightly change the spectral response of the detector. However, the size of the point-spread function (PSF) and the spacecraft dither minimizes the impact from the loss of a few grades in individual columns. We estimate that the uncertainty in the

¹ See <http://asc.harvard.edu/ciao/>.

² See <http://www.astro.psu.edu/xray/acis/recipes/index.html>.

TABLE 1
Chandra SOURCES IN NGC 6822

Source	R.A.	Decl.	R_{err} (arcsec)	PSF_sig (arcsec)	Counts
s01.....	19 44 16.391	-14 45 37.41	1.6	5.5	11
s02.....	19 44 19.627	-14 48 56.18	1.4	4.4	10
s03.....	19 44 19.767	-14 48 37.50	0.8	4.4	31
s04.....	19 44 23.295	-14 50 09.10	0.8	3.8	22
s05.....	19 44 24.994	-14 44 59.08	1.0	3.9	14
s06.....	19 44 26.819	-14 56 11.92	1.3	6.1	22
s07.....	19 44 27.376	-14 43 17.43	0.3	4.2	169
s08.....	19 44 28.431	-14 57 00.06	1.6	6.6	18
s09.....	19 44 29.311	-14 53 59.28	0.9	4.2	20
s10.....	19 44 30.082	-14 42 22.98	0.6	4.3	52
s11.....	19 44 31.983	-14 43 34.38	1.1	3.3	9
s12.....	19 44 32.036	-14 46 43.00	0.8	2.3	8
s13.....	19 44 34.351	-14 53 29.15	0.6	3.2	26
s14.....	19 44 37.324	-14 54 47.66	1.2	3.6	9
s15.....	19 44 37.827	-14 44 51.75	0.2	2.1	91
s16.....	19 44 37.951	-14 47 21.54	0.4	1.5	17
s17.....	19 44 38.961	-14 44 37.52	0.6	2.0	13
s18.....	19 44 40.135	-14 57 04.62	1.3	5.1	15
s19.....	19 44 40.327	-14 46 15.54	0.5	1.4	9
s20.....	19 44 42.034	-14 48 31.06	0.3	1.0	11
s21.....	19 44 42.575	-14 53 20.71	0.4	2.3	34
s22.....	19 44 43.569	-14 53 49.04	0.8	2.4	9
s23.....	19 44 43.661	-14 47 53.45	0.1	0.9	209
s24.....	19 44 43.878	-14 48 28.99	0.2	0.9	57
s25.....	19 44 44.629	-14 48 07.79	0.2	0.8	48
s26.....	19 44 45.724	-14 41 35.04	0.9	3.1	12
s27.....	19 44 47.477	-14 45 47.58	0.2	1.0	21
s28.....	19 44 48.189	-14 51 53.95	0.4	1.3	11
s29.....	19 44 49.486	-14 47 04.24	0.2	0.7	11
s30.....	19 44 51.882	-14 49 19.31	0.2	0.5	15
s31.....	19 44 51.883	-14 46 58.33	0.1	0.6	32
s32.....	19 44 52.485	-14 53 58.04	0.8	2.1	7
s33.....	19 44 54.568	-14 47 13.26	0.2	0.5	14
s34.....	19 44 56.604	-14 48 30.26	0.2	2.4	213
s35.....	19 44 59.039	-14 52 36.63	0.3	1.4	19
s36.....	19 44 59.644	-14 42 10.52	0.2	2.4	403
s37.....	19 44 59.687	-14 42 03.44	0.5	2.5	21
s38.....	19 44 59.911	-14 45 08.21	0.1	1.0	86
s39.....	19 45 00.357	-14 42 31.46	0.7	2.2	12
s40.....	19 45 01.569	-14 49 09.09	0.2	0.6	10
s41.....	19 45 04.300	-14 42 47.91	0.5	2.2	23
s42.....	19 45 04.487	-14 51 29.80	0.2	1.2	104
s43.....	19 45 04.717	-14 41 34.73	0.9	3.0	12
s44.....	19 45 05.050	-14 51 06.29	0.3	1.1	17
s45.....	19 45 05.275	-14 39 36.76	0.6	4.6	72
s46.....	19 45 05.512	-14 50 52.15	0.3	1.0	11
s47.....	19 45 07.497	-14 55 57.64	0.5	3.8	70
s48.....	19 45 07.686	-14 52 33.20	0.2	1.8	60
s49.....	19 45 08.366	-14 54 25.45	0.4	2.8	44
s50.....	19 45 08.537	-14 47 46.22	0.2	0.9	25
s51.....	19 45 10.514	-14 53 04.78	0.7	2.2	11
s52.....	19 45 10.534	-14 47 14.64	0.3	1.1	25
s53.....	19 45 11.852	-14 55 57.57	0.8	4.2	25
s54.....	19 45 12.912	-14 54 11.32	0.8	3.0	14
s55.....	19 45 13.015	-14 40 01.95	1.2	4.8	16
s56.....	19 45 13.057	-14 47 13.27	0.2	1.4	47
s57.....	19 45 14.791	-14 51 25.13	0.5	2.0	14
s58.....	19 45 14.905	-14 41 38.08	1.0	3.8	15
s59.....	19 45 16.794	-14 53 51.13	0.7	3.3	20
s60.....	19 45 18.832	-14 53 43.61	0.9	3.5	15
s61.....	19 45 19.763	-14 50 30.40	0.4	2.4	47
s62.....	19 45 21.541	-14 53 40.50	1.0	3.9	14
s63.....	19 45 22.250	-14 53 51.16	1.3	4.0	10

TABLE 1—*Continued*

Source	R.A.	Decl.	R_{err} (arcsec)	PSF_sig (arcsec)	Counts
s64.....	19 45 22.677	-14 40 23.88	0.3	5.8	385
s65.....	19 45 23.120	-14 48 30.58	0.8	2.6	11
s66.....	19 45 23.281	-14 44 47.23	1.0	3.3	12
s67.....	19 45 24.393	-14 43 10.01	0.7	4.2	37
s68.....	19 45 24.816	-14 44 52.72	0.5	3.6	51

NOTE.—Units of right ascension are hours, minutes, and seconds, and units of declination are degrees, arcminutes, and arcseconds.

response is increased by a few percent, which is smaller than statistical uncertainties for our sources. The traditional method of dealing with noisy columns, to remove all data from that column, produces obvious streaks in the data, whereas our method left a very smooth background.

Finally, we use A. Vikhlinin's software CLEAN55³ to further reduce the background. This method is also very effective at removing cosmic-ray afterglows, and so we did not explicitly remove events flagged as afterglow events.

The `lctrfct` source-finding tool is described in the Appendix. There we also describe a comparison background field, a 28.1 ks portion of ObsID 3388, the Chandra Deep Field–North (CDF-N) field. Using this field we compare our source-finding method with `wavdetect`, which is more commonly used in *Chandra* analysis. Although the raw source-finding positions are moderately accurate, we used an unweighted fit to a two-dimensional Gaussian to slightly improve the positional accuracy as discussed in the Appendix. These positions were compared with the Two Micron All Sky Survey (2MASS) catalog (as described below) and a world coordinate system computed to minimize the errors. Throughout this paper, positions are based on the 2MASS-derived coordinate system.

3. RESULTS

The `lctrfct` tool found 67 point sources with signal-to-noise ratios (S/Ns) greater than 2.4 on the ACIS-I array. Near the center of the detector an extended source with a diameter of about 8'' was found. The J2000.0 positions of these sources are listed in Table 1. The column R_{err} gives the radius that encloses the *Chandra* position with 90% confidence. Also listed are PSF_sig, the size of the PSF at this location, and the number of counts detected corrected for the PSF. Figure 1 shows the smoothed image with the sources located. Figure 2 shows a close-up image of each *Chandra* source.

Finally, source finding was run with PSF_sig set to a fixed value of 30''. This pass found two sources that are likely background galaxy clusters. Using the deep-field observation discussed in the Appendix, no clusters were detected in the 28.1 ks CDF-N exposure. By searching the full 50 ks from ObsID 3388, a known cluster is detected. From this we conclude that 1 ± 1 clusters is not an unreasonable number to expect, and this is consistent with the NGC 6822 data. Furthermore, these extended features are not associated with any H II regions in the galaxy. It is also convenient that one is found inside the D25 ellipse and the other outside, providing a weak argument for no association with NGC 6822. All these factors lead us to believe that these objects are background clusters of galaxies, and so they are not discussed further in this paper.

³ See <http://cxc.harvard.edu/cont-soft/software/clean55.1.0.html>.

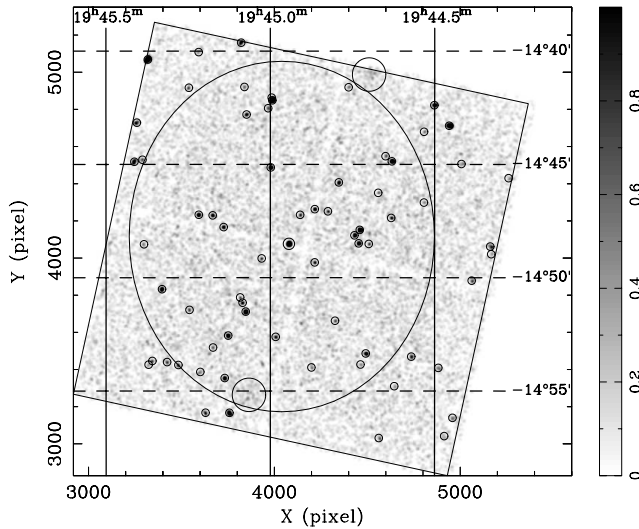


FIG. 1.—Full ACIS-I array image in the 0.5–8 keV band. The data have been smoothed to enhance the visibility of the sources. The small circles show the locations of the 67 point sources. The slightly larger circle near the center shows the (resolved) SN remnant. The large circles near the bottom and top of the image show the locations of the extended sources that could be background clusters of galaxies. The large ellipse shows the D25 ellipse. The D25 ellipse shows where the optical surface brightness of the galaxy is $25 \text{ mag arcsec}^{-2}$.

While comparing with the deep-field data, it is worth noting that 14 of the 503 objects in the Barger et al. (2003) sample are identified as stars, and in fact, two of the brightest 60 sources are stars. This is consistent with the number of stars that we identify in the NGC 6822 field.

3.1. Comparison to 2MASS Data

We compared the *Chandra* positions of the 67 point sources to the 2MASS⁴ catalog. Based on potential matches, we corrected the *Chandra* positions to match the 2MASS positions. This shift was $0''.22$ in right ascension and $0''.07$ in declination. This offset was found via an iterative process in which potential matches are found, an offset computed, and a new set of matches are searched for using the shifted coordinates. Here we describe the comparison process after the best shift has been computed and applied. In Figure 3 (*top*) we show a histogram of the distance from the *Chandra* position to the nearest 2MASS source. We also constructed a mirror list by reflecting the source positions through the center of the detector. In this list, each source has the same distance from the center of the detector as a true source but now in the opposite direction. This ensures that the sources have a similar spatial distribution as the true *Chandra* population. In Figure 3 (*bottom*) we show a histogram of the distance from the mirrored positions to the nearest 2MASS source.

The function shown in Figure 3 is the Poisson probability of getting one, and only one, source within a circle of radius r . This is given by

$$P(1; \mu) = \mu \exp(-\mu),$$

where

$$\mu = \sigma_d \pi r^2$$

⁴ See <http://www.ipac.caltech.edu/2mass/>.

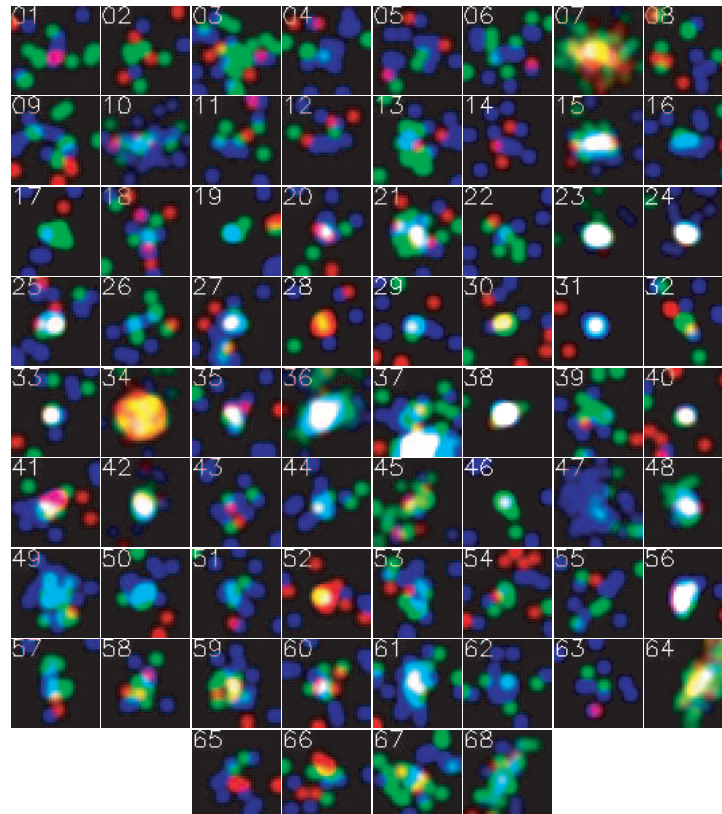


FIG. 2.—A $16''$ square region centered at the location of each *Chandra* source. Photons in the range 0.2–1.0 keV were colored red, 1.0–2.0 keV green, and 2.0–8.0 keV blue. Since the *Chandra* PSF degrades with the off-axis distance, sources near the edge of the CCD are spread over a larger area and are difficult to see in these fixed-size images.

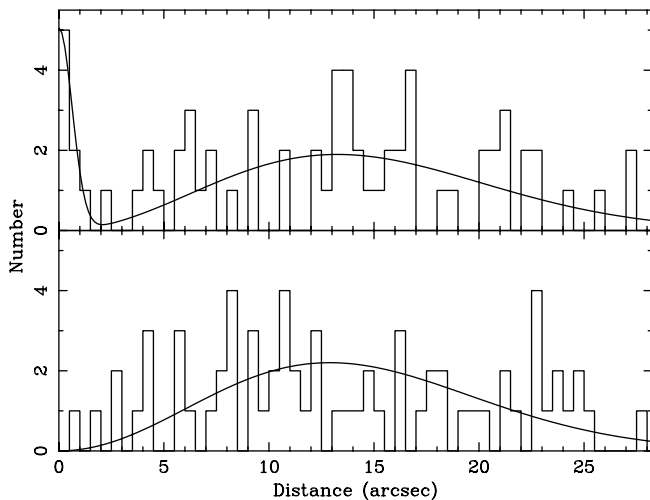


FIG. 3.—*Top*: Distance from the *Chandra* position to the nearest 2MASS source. *Bottom*: Distance from the mirrored *Chandra* position (see text) to the nearest 2MASS source.

and σ_d is the surface density of 2MASS sources. As can be seen from Figure 3 (*bottom*), this provides a very good approximation to the random distribution. Even though the peak is near $13''$, we find four sources with separations of less than $3''$, two less than $2''$, and one less than $1''$.

The data in Figure 3 (*top*) can also be fitted with the random distribution but with an additional Gaussian centered at zero. Clearly, the Gaussian represents the true matches, although 1 ± 1 could be due to chance. The eight sources with separations less than $2''$ were used to determine the coordinate offset.

Of the sources with possible 2MASS counterparts, we find that three, s07, s28, and s52, have colors consistent with unreddened main-sequence stars. They also have soft X-ray spectra and thus are likely foreground stars. Source s66 has 2MASS colors slightly off the main sequence, which is not unexpected, since faint stars in NGC 6822 add some background noise. Thus, s66 could be a foreground star or a background galaxy with a small intrinsic X-ray column. The remaining 2MASS sources s36, s41, s47, and s51 have colors suggesting some reddening. As we find below, sources s36 and s47 have extended optical counterparts and hard X-ray spectra that lead us to conclude that they are background active galactic nuclei (AGNs).

3.2. Comparison to Mosaic Data

We downloaded data from the NOAO/KPNO Mosaic-1 $8K \times 8K$ CCD. These data were obtained as part of the Local Group Survey⁵ led by P. Massey. In Figure 4 we show the Mosaic data near each *Chandra* location in three of the bands combined into a color image. The source s34 was resolved by *Chandra* into an object $8''$ across, and extended $H\alpha$ emission is seen at the same size and position in the Mosaic data. The sources s28 and s52 are clearly associated with bright foreground stars. The sources s07 and s66 are near, bright optical objects. The source s47 appears to be an edge-on galaxy. Finally, careful examination of s36 data suggested that it may be extended, which is confirmed with *Hubble Space Telescope* (*HST*) data (see below).

We used the `lextrct` source-finding tool to look for optical sources in each patch shown in Figure 4 (we excluded s34 from this analysis). We found 1205 sources in the 67 fields for an

⁵ See <http://www.lowell.edu/users/massey/lgsurvey.html>.

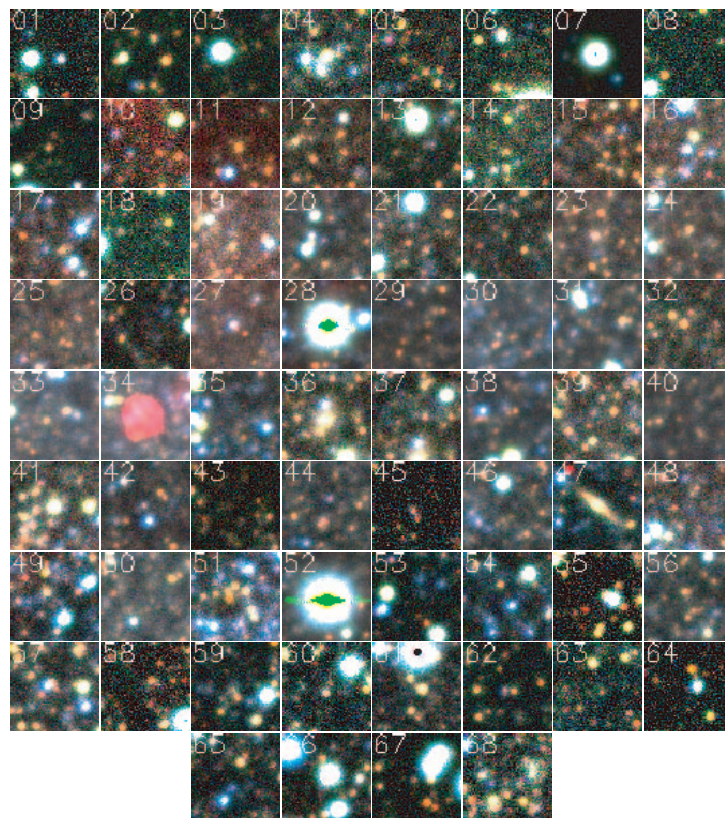


FIG. 4.—A $16''$ square region centered at the location of each *Chandra* source. The $H\alpha$ were colored red, the V band green, and the B band blue. The brightest sources, such as s28 and s52, saturated the detector in some bands, causing the artifacts.

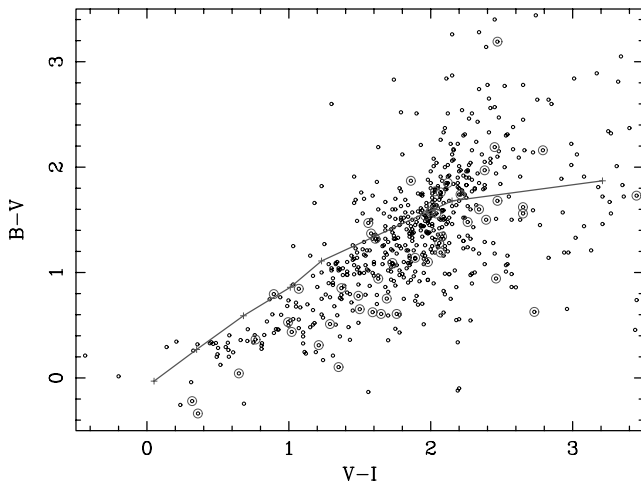


FIG. 5.—Optical color-color diagram for the fields shown in Fig. 4. Since many of the objects are faint and confused with other sources, there is a large scatter in the colors. All 637 sources that had measurable flux in all three bands are plotted here. The large circles show the color of the source closest to the *Chandra* position and less than $2''$ distant. The line shows the approximate location of the main sequence (reddened by $A_V = 0.8$ mag). We estimate that about 15 of the circled sources are true X-ray counterparts. It is clear that these sources do not populate a unique region of the diagram.

average of 18 per field. We then used the mirror source list constructed in the 2MASS analysis and searched fields about the mirrored positions. It is worth noting that s11 and s59 mirrored into each others' $16'' \times 16''$ fields, but not within $2''$. There are 1249 sources in this list. The fact that the number of sources is the same to within statistical errors shows there are no gross biases due to varying stellar density within NGC 6822. We next considered the source closest to the *Chandra* position, and there were 56 such sources within $2''$. In the mirror list we found 41 hits, indicating that about 15 of the *Chandra* hits are real counterparts to the X-ray source.

We estimated the B , V , and I magnitudes for all the sources in the *Chandra* patches. We kept only those sources for which we had good flux measurements in all three bands. This resulted in 637 sources in the main list and 643 in the mirror list. There were 50 fields that had a source within $2''$ (and 35 in the mirror list). An optical color-color diagram is shown in Figure 5. We can see that there is no obvious difference in the color distribution for the 50 sources in this sample that were within $2''$ and the field sources in the $16'' \times 16''$ patches.

3.3. Comparison to USNO-B1 Catalog

We matched *Chandra* positions to the USNO-B1 catalog (Monet et al. 2003). We also tried to compute a coordinate shift using this catalog but found that the resulting fit was not as good and the uncertainties were larger than what we found using the 2MASS catalog. This is not unexpected, since the USNO catalog is based on older data and hence is more affected by proper motion. Although an attempt is made to correct USNO positions for proper motion, the uncertainty in this motion introduces an error. For example, we find that the potential match for s47 had non-zero proper motion in the USNO catalog. Since s47 is extended and likely an external galaxy, this motion could be an artifact of fitting slightly different centroids for slightly different exposures and/or seeing conditions. The position was still accurate to better than $1''$ and consistent with the published uncertainties for the catalog.

We found eight potential matches in the USNO catalog. Seven of these also were the same as the 2MASS matches. The two

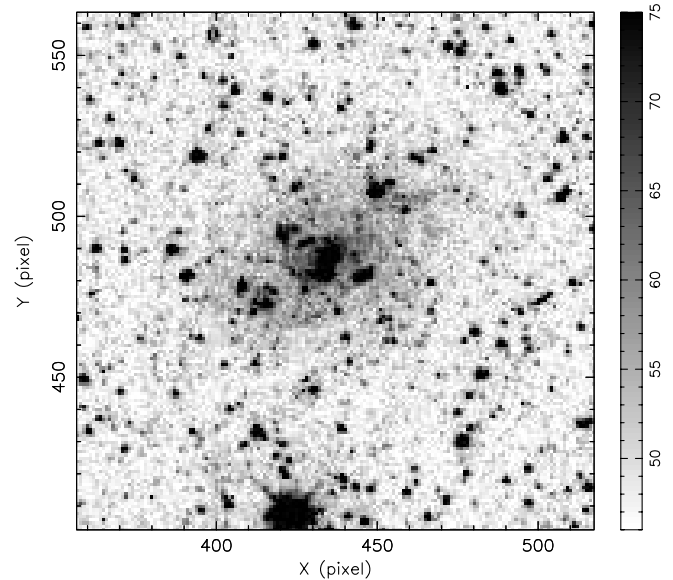


FIG. 6.—The $16'' \times 16''$ region centered on *Chandra* source s36 obtained with the *HST* WFPC2 camera. This is a 2600 s exposure obtained with the F555W filter. Cosmic rays have been removed.

differences were s04, which only matched a USNO source, and s51, which only matched a 2MASS source. From the Mosaic data seen in Figure 4, there are no bright optical sources in the s51 region. In the s04 area, Mosaic shows three moderately bright objects, which the USNO catalog did not fully resolve. At this time we feel that neither s04 nor s51 has a good candidate for a counterpart.

3.4. Comparison to HST Data

We searched the available *HST* WFPC2 associations⁶ for *HST* data in the NGC 6822 field. Due to the large number of stars in each image and the need to precisely register *HST* data, it is difficult to match *Chandra* sources to any particular *HST* source. The most interesting object is s36, shown in Figure 6. At first glance this appears to be very similar to the H II region shown in Wyder et al. (2000) called H IV, where H stands for Hubble. However, comparison with the ground-based data show that H IV is associated with very strong $H\alpha$ emission, whereas s36 is not. This, combined with the hard X-ray spectrum, leads us to conclude that s36 is most likely either a face-on spiral or elliptical galaxy.

The two moderately bright objects seen near the position of s16 in Figure 4 were both resolved by *HST* into two approximately equal brightness stars. In other words, there are actually four moderately bright stars near the *Chandra* position, none of which are close enough to be considered a potential match.

The *HST* observation of the area around s41 showed that the bright optical source seen in Figure 4 had clear diffraction spikes, indicating that it is unresolved by *HST*. Thus, s41 could be a star in NGC 6822 or a more distant QSO.

3.5. $\log N$ - $\log S$ Distribution

In Figure 7 we plot the number of sources brighter than a given count rate for the NGC 6822 field. We also show the $\log N$ - $\log S$ found from our analysis of the 28.1 ks exposure obtained from the deep-field observation. Since there is a slight variation in sensitivity across the field, analyzing an identical exposure

⁶ See <http://archive.stsci.edu/hst/wfpc2/index.html>.

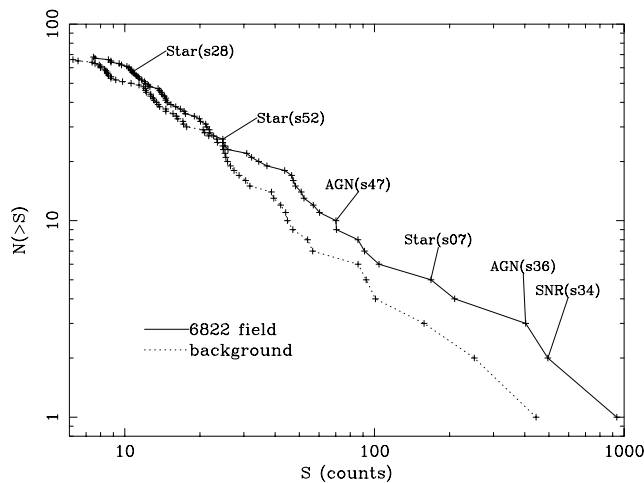


FIG. 7.—The log N -log S distribution for NGC 6822. The log N -log S distribution for a background observation with an identical exposure time is also shown. The brightest two NGC 6822 sources were dithered off the detector. Here we have corrected for this.

from a different field provides a simple way to take this into account. As can be seen from the figure, there is no large excess of sources in the NGC 6822 field. By fitting a power law to the distribution above 10 and computing the value at 10 counts (as a reasonable completeness level), we find 61 sources in the NGC 6822 field and 56 in the background. Thus, we conclude there are 5 ± 8 sources local to NGC 6822, where 8 assumes purely Poisson fluctuations in the field.

We can also estimate the number of NGC 6822 sources from our data if we assume that the spatial density of background sources is uniform across the field. By comparing the number of sources inside and outside the D25 ellipse we find that the inner region contains an excess of 6.7 ± 9.5 sources. Due to vignetting and the increase in size of the PSF off-axis, one expects greater sensitivity and hence more sources near the center of the field. We ran the same source finding on the 28.1 ks deep-field north observation and found 66 point sources. We rotated the D25

ellipse so that it covered the same detector region. For this field there was an excess of 15.7 ± 9.3 sources inside the pseudo D25 ellipse. From this we conclude that there is no evidence for an excess of X-ray sources in NGC 6822. In fact, this test is consistent with a slight deficit of sources within the D25 ellipse.

One possible way to account for a deficit of sources is to assume that NGC 6822 contains enough gas to significantly absorb X-rays from sources behind it. This would result in fewer detected background sources, and NGC 6822 sources would make up the difference. Of course, this requires a coincidence to get the numbers to approximately cancel. The largest neutral hydrogen column measured by de Blok & Walter (2000) was $3 \times 10^{21} \text{ cm}^{-2}$, which is larger than the Galactic column of about $1 \times 10^{21} \text{ cm}^{-2}$ (Dickey & Lockman 1990). Assuming a $\Gamma = 1.7$ spectral index, increasing the column from 1×10^{21} to $4 \times 10^{21} \text{ cm}^{-2}$ decreases the ACIS-I count rate by about 15% using standard (cosmic) abundances. Thus, a source behind NGC 6822 and detected at 10 counts would be seen at 11.5 counts if this excess column were removed. Going back to our 28.1 ks CDF-N background image, we find that there are 48 sources above 11.5 counts. Since only these sources would have been detected in the NGC 6822 field, this implies that as many as 13 (61–48) sources are from NGC 6822 itself. Since the actual abundance of metals in NGC 6822 is smaller and we used the maximum column, the actual impact on the X-ray count rate would be smaller. Thus, depending on the assumptions made about the column, the number of sources can range from 5 to 13, or 9 ± 4 . Thus, we find that there are $9 \pm 4 \pm 8$ sources, where the first error represents a systematic uncertainty depending on the method and the second the statistical error.

3.6. Diffuse Emission

We searched for diffuse emission in the NGC 6822 field. First, the image was read into a grid with $4''$ pixels. Next, pixels' near known sources were flagged to be excluded from the analysis. Finally, the image was aggressively smoothed (nearest neighbor average applied 10 times). The resulting image is shown in Figure 8 (*left*). By comparing the counts inside and outside the D25

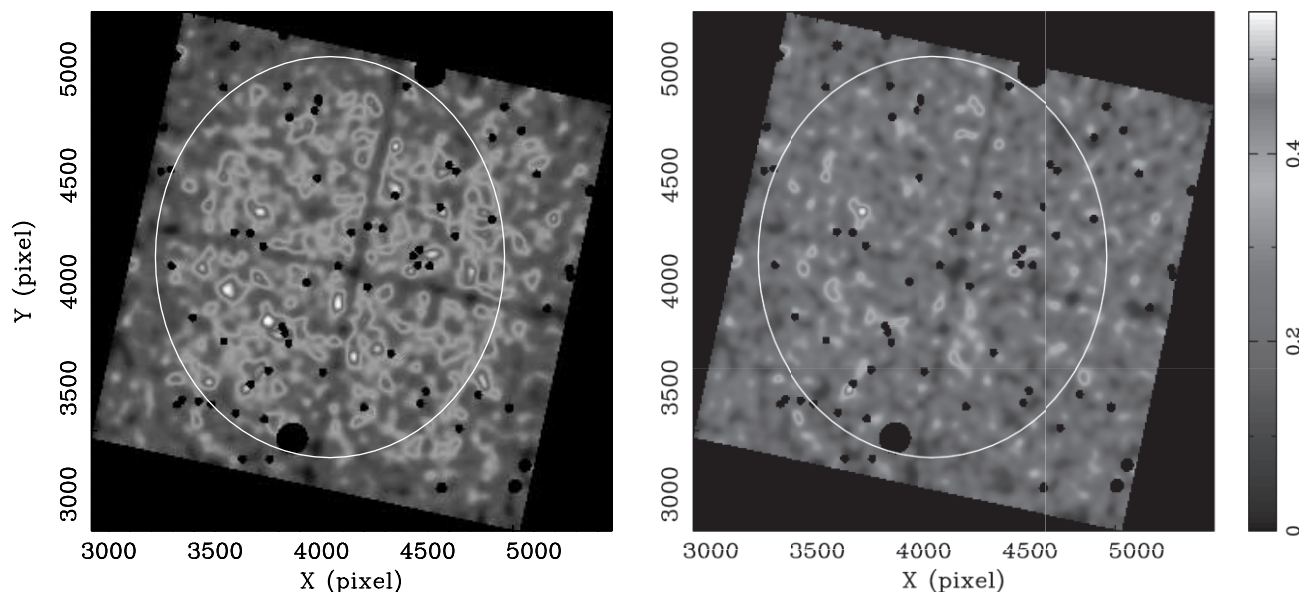


FIG. 8.—*Left*: Point-source removed, highly smoothed image of the full 28.1 ks data set. Notice that flux inside the D25 ellipse is higher than outside. *Right*: Same as the left panel, except now 6.5 ks of slightly higher instrumental background have been removed. The excess count rate inside the D25 ellipse is now much less obvious.

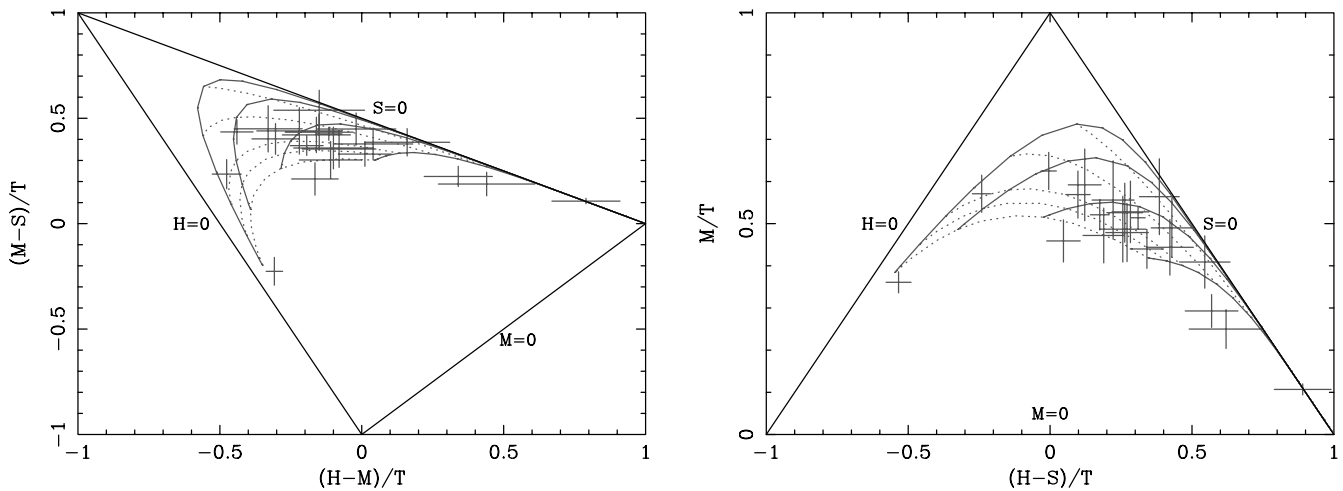


FIG. 9.—*Left*: X-ray color diagram for the sources in the NGC 6822 field having more than 30 counts total. The three straight lines show the loci at which the counts in one of the bands go to zero. The requirement that all rates be positive forces all data values to lie within the triangle. The solid curves show where the power-law spectra with photon indices of $\Gamma = 1.0, 2.0, 3.0$, and 4.0 would lie. The dotted curves show the columns of 1×10^{20} , 1×10^{21} , 2×10^{21} , 5×10^{21} , and 1×10^{22} . *Right*: Same data but rotated so that the $M = 0$ line lies along the X -axis.

ellipse, we find an excess of 3010 ± 180 counts inside D25. This excess corresponds to an average of 1.3×10^{-3} counts pixel $^{-1}$.

However, the observation contained some intervals in which the background increased by up to a factor of 4. These modest background flares have little impact on the point sources and so have been ignored so far. To test the impact of these flares on the diffuse emission, we excluded about 6.5 ks of high background and repeated the above analysis as shown in Figure 8 (*right*). The D25 excess is now only 830 ± 140 counts. In rough terms, 75% of the excess occurred during 25% of the observation. We note that contamination on the ACIS filter is thicker near the edges; thus, it is possible that this extra thickness reduces the particle background outside the D25 ellipse. Due to vignetting, the X-ray background is higher near the center of the field. To check this effect, we considered a 21.6 ks time slice from the deep-field observation that showed no detectable background flares. Using an ellipse that has the same size as the NGC 6822 ellipse and covers the same part of the detector, we find an excess of 400 ± 134 counts. Subtracting this excess from the NGC 6822 excess leaves 430 ± 200 counts in 21.6 ks. Given the large corrections that we had to apply to obtain this value, we do not feel that this is a positive detection of diffuse emission.

3.7. X-Ray Variability

We ran the Kolmogorov-Smirnov (K-S) test on all the X-ray light curves and found nine sources (s03, s06, s08, s12, s16, s32, s54, s59, and s62) that had a K-S probability of being consistent with a constant rate of less than 5%, where 3.4 sources would be expected by chance. The most variable source by this test was s59, which showed a flare near the end of the observation. The next most variable source was s08, for which 44 counts occurred in the first half of the observation and only 19 in the second.

We also computed the power spectra of all the sources. We plotted the power spectra using the Leahy normalization and found that sources s31, s34, and s64 all showed peaks in excess of 25, a threshold that warrants further attention. All three sources lie near the edge of a CCD, and the peaks matched the dither period as the spacecraft motion moved the source on and off the detector. Thus, none of these peaks were real. The largest non-dither-related peak was for s36 and had a peak value of 24.3 at a period of 156 s. Since a peak of this amplitude is expected by

chance about once in our entire sample, we do not feel that it is real.

3.8. X-Ray Colors

In Figure 9 we show an X-ray color diagram. In the left panel we use the colors as defined in Prestwich et al. (2003), where S is the 0.5–1.0 keV rate, M is the 1–2 keV rate, H is the 2–8 keV rate, and T is the total 0.5–8 keV rate. We also plot three lines showing the location at which the flux is zero in each of the three bands. Since the flux should be positive, all sources should lie within the triangular region thus created, although statistical errors on background subtraction can result in some sources being slightly outside. As you move across the diagram from the $M = 0$ line to the opposite vertex, the fraction of the flux in the M band increases from zero to 100%. A source with flux only in the S band (i.e., very soft) appears at the bottom center, whereas the hardest sources appear at the right halfway up. Although we plot the errors aligned with the axes, we note that since the M band appears in both ratios, the errors are correlated and so should be plotted as rotated ellipses. Dividing by the total also introduces some correlations, but since this band contains the largest number of counts it will not be the largest contribution to the error.

A better way to plot the same data is to rotate the diagram in color space. If we place the $M = 0$ line along the X -axis, then the X -coordinate becomes $(H - S)/T$, which represents a simple hardness with the widest separation in the bands. The Y -coordinate becomes M/T , which represents how centrally peaked the spectrum is. Now sources with flux in the S band only appear on the far left and sources with H -band flux only on the far right. We note that it is unusual for an X-ray spectrum to be confined to just the M band with no S and H flux, with the top corner thus not populated. Hence, a population of X-ray spectra forms an arc across the middle of the diagram. We also note that since $H - S$ and M are independent, the errors will also be independent in this space.

The softest source is the SN remnant s34, and the next softest is s07, which appears to be a nearby star. The third softest source is s64, which is also the brightest. The hardest source is s47, which appears to be associated with an edge-on galaxy based on ground-based data. The next hardest source is s36, which looks

TABLE 2
SPECTRAL FITS

SOURCE	POWER-LAW MODEL				MEKAL MODEL				
	nH^a	Γ	Flux ^b	C	nH^a	kT (keV)	Abun.	Flux ^b	C
s64.....	$4.1^{+2.0}_{-1.7}$	$3.39^{+0.73}_{-0.61}$	$4.5^{+4.0}_{-1.6}$	248.7	2.0 ± 1.3	$1.20^{+0.59}_{-0.35}$	$0.000^{+0.075}_{-0.035}$	$2.2^{+0.6}_{-0.4}$	246.1
s34.....	$2.1^{+2.1}_{-1.6}$	$4.80^{+1.29}_{-0.97}$	$3.1^{+6.6}_{-1.7}$	199.9	$0.0^{+0.7}_{-0.0}$	$0.58^{+0.07}_{-0.10}$	$0.071^{+0.076}_{-0.040}$	$0.95^{+0.03}_{-0.06}$	186.1
s36.....	$3.0^{+1.3}_{-1.2}$	1.70 ± 0.26	$2.2^{+0.3}_{-0.2}$	411.2	2.3 ± 1.0	$8.8^{+12.7}_{-3.6}$	$0.00^{+0.51}_{-0.00}$	2.0 ± 0.1	411.5
s23.....	2.0 ± 1.5	1.94 ± 0.36	$0.99^{+0.21}_{-0.16}$	306.3	1.2 ± 1.1	$4.9^{+5.3}_{-1.8}$	$0.00^{+0.26}_{-0.00}$	0.86 ± 0.08	305.3
s07.....	$4.9^{+2.4}_{-1.4}$	$4.93^{+1.26}_{-0.98}$	$2.9^{+6.9}_{-1.7}$	171.7	$1.3^{+2.0}_{-1.3}$	$0.82^{+0.30}_{-0.26}$	$0.062^{+0.073}_{-0.046}$	$0.54^{+0.35}_{-0.17}$	167.6
s42.....	2.7 ± 2.1	$2.38^{+0.62}_{-0.56}$	$0.50^{+0.26}_{-0.13}$	205.8	$1.4^{+1.7}_{-1.4}$	$2.8^{+2.9}_{-1.1}$	$0.00^{+0.70}_{-0.00}$	$0.38^{+0.09}_{-0.05}$	205.1
s15.....	$0.1^{+2.3}_{-0.1}$	$1.13^{+0.51}_{-0.36}$	0.47 ± 0.11	273.4	$1.1^{+1.5}_{-1.1}$	80^{+95}_{-69}	$9.5^{+9.5}_{-2.74}$	0.48 ± 0.05	273.2
s38.....	$0.1^{+2.0}_{-0.1}$	$2.04^{+0.63}_{-0.47}$	$0.34^{+0.13}_{-0.08}$	229.1	$0.0^{+1.2}_{-0.0}$	$4.6^{+4.0}_{-2.0}$	$0.63^{+2.74}_{-0.63}$	0.31 ± 0.05	228.5

^a In units of 10^{21} cm^{-2} .^b In units of $10^{-13} \text{ ergs cm}^{-2} \text{ s}^{-1}$.

like a face-on galaxy in *HST* data. The next two hardest sources are s10 and s49. These could be either background AGNs or HMXBs. All the other sources have canonical X-ray colors typical of background AGNs.

3.9. X-Ray Spectra

Eight sources had enough counts to attempt a spectral fit. Using `lextract`, we extracted all counts out to a radius of 2.5 times PSF_{sig}. Response matrices were calculated using CIAO. The background was estimated by removing all the known sources (and the two cluster-like objects). The actual spectral fits were done using XSPEC (Arnaud 1996). We fit unbinned spectra using XSPEC's C -statistic. We show results of the spectral fits in Table 2. For an assumed power-law model, the columns nH , Γ , Flux, and C give the absorbing column, photon index, flux, and C -statistic. For a MEKAL model, the columns nH , kT , Abun., Flux, and C give the absorbing column, temperature, abundance, flux, and C -statistic. We tested whether a model was statistically acceptable by grouping the data to 10 counts per bin and then using the χ^2 statistic. For this statistic the only model that we could rule out at the 98% confidence level was the power-law model for s34. For all other spectra, both models provided fits that were acceptable at the 90% level, although for s07 the MEKAL model was favored.

A single-temperature MEKAL model is slightly better than the power-law model for source s34. Since this source is clearly the SN remnant in NGC 6822, we expect the column to be close to the Galactic value of $1 \times 10^{21} \text{ cm}^{-2}$. A column this large is statistically ruled out at better than 90% confidence. This is an indication of a second temperature component to the spectrum. For further discussion of this spectrum, see Kong et al. (2004).

4. INDIVIDUAL SOURCES

In previous sections we discussed various data sets and mentioned sources that stood out in each set. In this section we discuss individual sources and the information gleaned by examining all the data. Since we have not obtained optical spectra of potential counterparts, we note that all potential identifications should be regarded as tentative.

4.1. s07

This is a bright 2MASS source, and the $J - K$ color suggests a K7 star. Assuming the star is on the main sequence, we find a distance of 240 pc. Based on a K7 spectral type, we extrapolate a V -band magnitude of 15.1, which is consistent with the 15.3 that we estimated from the Mosaic data. The X-ray color is fairly soft

(0.82 keV MEKAL), which also favors coronal emission. The 0.5–8 keV flux of $5.4 \times 10^{-14} \text{ ergs cm}^{-2} \text{ s}^{-1}$ implies a luminosity of $3.7 \times 10^{29} \text{ ergs s}^{-1}$. Although the luminosity is a bit high, everything is consistent with coronal emission from a normal star in our galaxy.

If s07 was actually in NGC 6822, then the absolute magnitude would be -8.2 and the X-ray luminosity would be $1.6 \times 10^{36} \text{ ergs s}^{-1}$. Thus, the optical is brighter than typical K supergiants ($M_V = -5.6$). The low temperature and brightness would imply a large surface area, which would be inconsistent with Roche lobe overflow, which restricts the size of stars. These facts make it very unlikely that s07 is in NGC 6822.

4.2. s28

A bright foreground star totally dominates the optical image. The 2MASS color suggests a K0 star, which would be 190 pc away. We extrapolate a V -band magnitude of 12.25. The star saturated the Mosaic CCD, but by extracting counts over a large region we estimate $V = 12.4$, which agrees with the extrapolated value to within our uncertainties. The X-ray color is soft. Using the C -statistic, we find a 0.6 keV MEKAL with a 0.5–8 keV flux of $2.7 \times 10^{-15} \text{ ergs cm}^{-2} \text{ s}^{-1}$. The X-ray luminosity would be $1.2 \times 10^{28} \text{ ergs s}^{-1}$. Everything is consistent with coronal emission from a normal star in our galaxy.

4.3. s34

This source is resolved in both *Chandra* and ground-based $H\alpha$ data to an object with a $4''$ radius. This corresponds to a radius of 10 pc at the distance of NGC 6822. This object had been identified as a candidate SN remnant in the survey by D'Odorico et al. (1980). The X-ray spectrum is soft and well fitted by a MEKAL-type model. These facts lead us to conclude that this source is a SN remnant in NGC 6822. This is the only X-ray source in the field that we are confident is actually associated with NGC 6822. For further discussion, see Kong et al. (2004).

4.4. s36

The 2MASS $J - K$ color is 1.66, which makes this source redder than an M7 star. Thus, it cannot be a foreground star, as it would not be as highly reddened. The X-ray spectrum is well fitted by a $\Gamma \sim 1.7$ power law, which is a typical AGN spectrum. The *HST* data show that the source is near an extended object. The Mosaic data do not show an excess of $H\alpha$, and so the extended object is unlikely to be an H II region within NGC 6822. All these facts lead us to conclude that this source is most likely a background AGN.

4.5. s47

The 2MASS $J - K$ color is 1.62, which makes this source redder than an M7 star. Like s36, this cannot be a foreground star. This source had the hardest X-ray spectrum in this field, likely due to a large column. The Mosaic data clearly show an extended source that resembles an edge-on galaxy. It is likely a background AGN.

4.6. s52

A bright foreground star totally dominates the optical. The 2MASS color suggests a G5 star, which would be 250 pc away. We estimate a V -band magnitude of 11.92. The star saturated the Mosaic CCD, but by extracting counts over a large region we estimate $V = 11.9$, which agrees within our uncertainty. The X-ray color is soft. Although we did not have enough counts for a reliable spectral fit, we did try using the C -statistic to fit a 0.5 keV MEKAL with a 0.5–8 keV flux of 6.7×10^{-15} ergs cm $^{-2}$ s $^{-1}$. The X-ray luminosity would be 5.0×10^{28} ergs s $^{-1}$. Everything is consistent with coronal emission from a normal star in our galaxy.

4.7. s64

This unremarkable source warrants mention, since it is the brightest source in the field and was seen with both *Einstein* and *ROSAT*. The X-ray spectrum is fairly soft, and either a $\Gamma = 3.4$ power-law model or a 1.2 keV MEKAL model fits. The steep power-law index suggests a thermal origin for the emission, but the lack of lines either implies a low metal abundance or a power law. A disk blackbody model with $kT = 0.6$ keV also fits. Thus, we conclude that for our brightest source the X-ray spectrum is somewhat ambiguous.

It is worth noting that the spacecraft dither caused this source to be moved on and off the instrument. An attempt has been made to correct for this, but we feel that the positional uncertainty could be much larger than typical. The Mosaic data show a very faint red object within the *Chandra* error circle. However, there is also a brighter, bluish object slightly outside the formal error circle that cannot be totally ruled out as a counterpart. The V magnitude of the brighter object is 20.8, and it was not detected in the 2MASS data. The $B - V$ value is 0.6, corresponding to a G0 star, which would place the source at the unlikely distance of 20 kpc. Thus, it is either highly reddened or not a star. The X-ray column implies that A_V is 2 mag, which would make the corrected brightness and colors marginally consistent with a B-type star at the distance of NGC 6822. Thus, this source could either be a background QSO or a Be X-ray binary in NGC 6822, and we recommend that an optical spectrum be obtained.

4.8. s66

The 2MASS color suggests a K5 star, which would be 1000 pc away. We extrapolate a V -band magnitude of 17.5. We estimate $V = 17.0$ from the Mosaic data. The X-ray spectrum did not have enough counts to obtain a reliable fit. Fitting a thermal spectrum gave a temperature of 60 keV with a 0.5–8 keV flux of 9.3×10^{-15} ergs cm $^{-2}$ s $^{-1}$. The X-ray luminosity would be 1.1×10^{30} ergs s $^{-1}$. The hard X-ray spectrum, large distance, and hence the large inferred X-ray luminosity, all argue against a foreground star, although none of these arguments are conclusive.

If the star is in NGC 6822, then it would have $M_V = -6.5$, with some uncertainty due to reddening correction, and could be a supergiant of virtually any spectral type. The X-ray luminosity would be 2.8×10^{35} ergs s $^{-1}$. Thus, it is possible that the system

is a faint wind-fed HMXB. There is no strong column in the X-ray data, but if the wind is weak this would not be required. We also cannot rule out a background AGN. Again, an optical spectrum would be useful.

5. DISCUSSION

Including both systematic and statistical errors, we find an excess of $9 \pm 4 \pm 8$ sources in the *Chandra* NGC 6822 field. Grimm et al. (2003) have shown that the HMXB population of a galaxy scales by the star formation rate (SFR). For the Milky Way, they used a total SFR of $0.25 M_\odot$ yr $^{-1}$ and found about 80 HMXBs above a luminosity of 10^{35} ergs s $^{-1}$. The SFR in NGC 6822 is $0.021 M_\odot$ yr $^{-1}$ (see van den Berg 2000, p. 170). Applying this simple scaling estimate implies that there would be about seven HMXB systems in NGC 6822. The number of LMXBs scales by the total mass of the galaxy. The mass of NGC 6822 is about 1% of the mass of the Milky Way, and since the Milky Way contains about 100 LMXBs, we would expect one LMXB in NGC 6822. The total number of predicted sources is in good agreement with the estimated number detected.

Diffuse emission was not detected with high confidence. Here we use the measured value of 430 ± 200 counts in 21.6 ks to set a scale. If we assume that this corresponds to optically thin emission at 1 keV, then the total luminosity is 4×10^{36} ergs s $^{-1}$. If we assume that there are 2×10^9 stars in NGC 6822 and that this emission is due to coronal emission, then the average star would be radiating at a rate of 2×10^{27} ergs s $^{-1}$. Since X-ray emission from our Sun varies from 3×10^{26} to 5×10^{27} ergs s $^{-1}$ (Peres et al. 2000), the possible diffuse emission is not inconsistent with this. We can infer that NGC 6822 is not dominated by young rapidly rotating stars, which would emit more coronal X-rays than we see.

The SN remnant is the only source for which we have high confidence that it is really associated with NGC 6822. It was discovered in *Einstein* data with a count rate of 1.4 counts ks $^{-1}$ (Markert & Donahue 1985). Note that the *Chandra* flux corresponds to a estimated *Einstein* rate of 1.5 counts ks $^{-1}$. Markert & Donahue (1985) noted that the source was coincident with the only candidate SN remnant in the survey by D'Odorico et al. (1980). Eskridge & White (1997) reported on a *ROSAT* observation of NGC 6822, and again the SN remnant was detected. They found that a 0.56 keV Raymond-Smith model provided an acceptable fit to the data and with this spectrum predicted an *Einstein* count rate of 1.3 counts ks $^{-1}$, in agreement with the Markert & Donahue (1985) result. Unfortunately, they compared to a table published in Fabbiano et al. (1992) that reported the count rate from this source to be 4.21 counts ks $^{-1}$. In order to resolve this discrepancy, we reanalyzed the *Einstein* data. Fabbiano et al. (1992) used a 60'' extraction radius, and when using that we find an excess of 143 ± 36 counts, or about 4.2 counts ks $^{-1}$. Markert & Donahue (1985) used an 18'' (we assume radius) circle, and for this size region we find 40 ± 12 counts, or 1.2 counts ks $^{-1}$. We can more closely reproduce the Markert & Donahue (1985) number by adjusting the unspecified size of the background region. In other words, we can reproduce the results from both papers, and so the difference is entirely due to the size of the extraction region. The *Einstein* background appears to be slightly higher between 18'' and 60'' from this source. It is worth noting that there were no other detected *Chandra* sources within the larger Fabbiano et al. (1992) region and that the slight enhancement is not detected in the *Chandra* data. We conclude that s34 has not shown significant variability between 1979 and 2002 and is the (only known) SN remnant in NGC 6822.

The author would like to thank Doug Swartz for many detailed comments on the manuscript. This publication makes use of data products from the Two Micron All Sky Survey, which is a joint project of the University of Massachusetts and the Infrared Processing and Analysis Center, California Institute of Technology, funded by the National Aeronautics and Space Administration and the National Science Foundation.

APPENDIX A SOURCE FINDING

Our source-finding tool is part of a command-line driven FORTRAN software package that dates from the early 1980s. It was first used to find sources in data from the Low Energy Telescopes on *EXOSAT*, hence the name *lextrct*.

The original algorithm was coded by T. McGlynn, was modified by K. Arnaud, and is currently maintained by A. Tennant. The formula to calculate the uncertainty in the source counts, i.e., the noise, was derived by M. Weisskopf. We describe the *lextrct* source-finding method in detail here. Other features of the software system are described briefly in help files as part of the complete package, available by request from the author.

A1. BASIC ALGORITHM

For each test position (pixel) within a user-defined search area, the algorithm compares the spatial distribution of detected events to the distribution predicted by a model PSF centered on the test position. The model PSF is stored as a two-spatial-dimension data array; it does not require an analytic functional form. The PSF model is normalized to unity so that each pixel, (i, j) , is characterized by the fraction of the PSF, $f_{i,j}^{\text{PSF}}$, contained within that pixel. Let $C_{i,j}$ be the total number of events detected in the pixel; then

$$C_{i,j} = S f_{i,j}^{\text{PSF}} + B_{i,j}, \quad (\text{A1})$$

where S represents a to-be-determined scale factor and $B_{i,j}$ represents the local background. Assuming that the background is constant over the small region in which $f_{i,j}^{\text{PSF}}$ is significantly above 0, $B_{i,j} \equiv B_{\text{est}}$, and summing over the region of N pixels

$$\sum_{i,j} C_{i,j} = S \sum_{i,j} f_{i,j}^{\text{PSF}} + N B_{\text{est}}. \quad (\text{A2})$$

Let C be the total number of counts in the region and $B = N B_{\text{est}}$ be the total background. Then, since $\sum_{i,j} f_{i,j}^{\text{PSF}} \equiv 1$, we have

$$S = C - B, \quad (\text{A3})$$

and we see that the scale factor S is the number of source counts in the region.

The algorithm is illustrated in Figure 10, which shows a clear detection of a source of about $S \sim 20$. Here $f_{i,j}^{\text{PSF}}$ is the abscissa and $C_{i,j}$ is the ordinate. An unweighted least-squares fit to a straight line gives the slope S and intercept B_{est} . Although the slope is determined by an unweighted fit, the uncertainty on the slope is estimated by the standard propagation of errors, assuming the square root of counts as the error on the data. The S/N is the slope divided by the error on the slope.

A potential source is any test position in which the S/N exceeds a user-defined threshold value. To ensure only one detection for each source, it is required that the test position be a local maximum in the estimate of source counts. This is preferable to

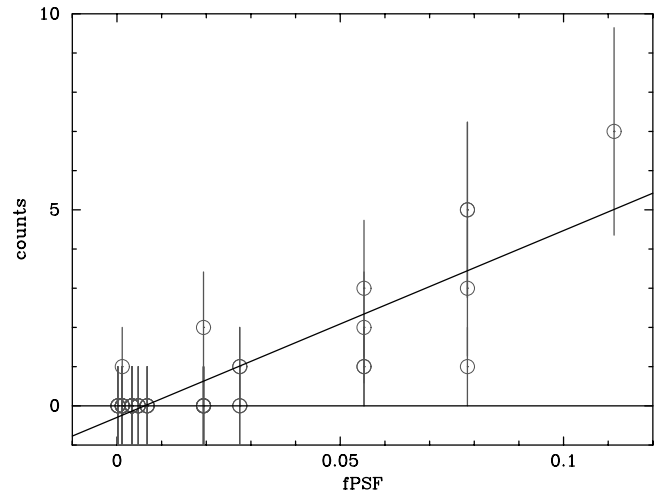


FIG. 10.—Number of counts in each pixel plotted against the f^{PSF} within that pixel. The line is the unweighted least-squares fit to the data. The fact that it slopes upward shows that there is a source at this location. Notice that the intercept is negative, suggesting that the PSF model is not totally correct.

requiring it be a local maximum in the S/N map, since a true source has a similar width in both the signal and the noise maps, and its peak in S/N is therefore not as prominent as in either of these component maps.

The optimum S/N threshold value is determined by inspection of the S/N distribution for all pixels in the search area (which can be the entire detector field of view). This distribution will have a Gaussian noise peak at S/N = 0 with an extension due to true sources at higher S/N. In the center of the detector field, where *Chandra* is count-limited, a minimum S/N = 2.4 is adequate to find all sources. The PSF size increases with off-axis position, and the background becomes more important. In the most extreme cases, the uncertainty in the background dominates, and a S/N threshold of 2.4 could include a 2.4σ fluctuation in the background. To minimize these statistical fluctuations appearing as false positives, we further require that source counts exceed 5 times the uncertainty in the background.

Since the source-finding method operates on an image with discrete pixels, sources are only located to an accuracy of a single pixel. The position is then refined in *lextrct* by computing the center of mass of the event distribution. Since the PSF has a roughly bilateral symmetry, this refinement ensures that the final position will be correct on average. The accuracy is limited by the fact that all events are weighted equally. Thus, events far from the center of the PSF have a larger impact on the location of the center than events near the center (of course, there are typically many more events near the center). A slight improvement in centroid accuracy can be achieved by fitting the raw data to a two-dimensional Gaussian function. With this model, events far from the PSF center now have a much smaller impact on the source location. Effectively, the position is now more strongly affected by nearby events likely to be from the source rather than more distant events that are likely to contribute to the background. This results in slightly more accurate source positions. This fitting is currently run post facto but is robust enough to run autonomously on typical source lists. In the future, this final fitting step may be included directly in the source-finding routine instead of being implemented as an optional intermediate operation.

Although the slope is an estimate for the number of source counts, the fact that the PSF model is not exact can introduce an error. This becomes obvious for sources containing a large number of counts, where statistical errors can be smaller than deviations

of the model PSF from the true PSF. For high count rate sources, the best-fit line will no longer intersect the origin at the background level but is biased to reduce errors in the pixels containing a larger number of counts. This change in the background level directly impacts the slope. We find that a safer way to estimate the source flux is to use a simple counts in a box approach. Source counts are estimated by counting the counts in a circle out to 2.5 times the effective width of the model PSF, called the PSF_sig . The area-weighted background is estimated from an annulus extending from 2.5 to 6 times the PSF_sig . Finally, the total source count is then corrected for the fraction of the PSF falling inside the inner circle.

A2. APPLICATIONS

The `lextrct` source-finding method was tested on ObsID 3388, an observation of the CDF-N that was obtained at a similar epoch as the NGC 6822 observation and that had a similar instrument configuration. To compare with the NGC 6822 data set, the data were processed in exactly the same way, and a 28,100 s portion was selected from the beginning of the observation. Figure 11 shows the central region of this field. The 184 sources from the 2 Ms point-source catalog (Alexander et al. 2003) that lie within this field are plotted with the smallest circles. Since the catalog is based on a 70 times longer exposure, we assume that it is reasonably complete. The `lextrct` source finding was run with three different models for the PSF.

A2.1. Circular Gaussian Model PSF

For computational expedience, the default PSF model in `lextrct` is a circular Gaussian in which the width of the Gaussian, σ , increases as a two-parameter quadratic function of the off-axis distance r : $\sigma = a + br^2$. This is a reasonable representation of the core of the true *Chandra* PSF within $\sim 10'$ of the aim point and has the advantage that it is analytically differentiable. It has been found that defining σ to be the radius that encloses 68% of the events increases the S/N for sources and for any given threshold increases the number of sources found. It is worth remembering that, for a two-dimensional Gaussian, 68% of the flux is enclosed when $r = 1.51\sigma$, and hence the model PSF is about 1.5 times larger than the true. To see how having a model larger than the true PSF helps, consider Figure 10. As you increase the PSF size, the values near the peak become lower, and so f^{PSF} moves closer to the origin. Of course, the number of counts in the pixel does not change, and so the slope increases. As you move away from the peak, the f^{PSF} increases. Again, this increases the slope. Thus, the total effect is to increase S_{est} , decrease the background estimate, and hence increase the S/N. Of course, if the size is increased too much, then nothing distinguishes source from background. In this case, the best-fit line becomes uncorrelated, with the uncertainty slope exceeding the value of the slope, and the S/N drops.

The minimum S/N threshold for a source detection depends on several factors, such as the size of the PSF, the image pixel size, and the background rate. One way to estimate a threshold is to construct a histogram of the S/N distribution for the field being searched. Typically, this histogram can be decomposed into a Gaussian centered near zero with an exponential tail. The Gaussian is due to random fluctuations in the background, whereas the exponential is due to real sources (and their wings). For our sample field, the entire area considered for a source may contain a single count, and hence the S/N for the background is often degenerate and thus non-Gaussian. However, the exponential tail is seen above 2.0. A S/N threshold of 2.0 resulted in 27 sources, shown in

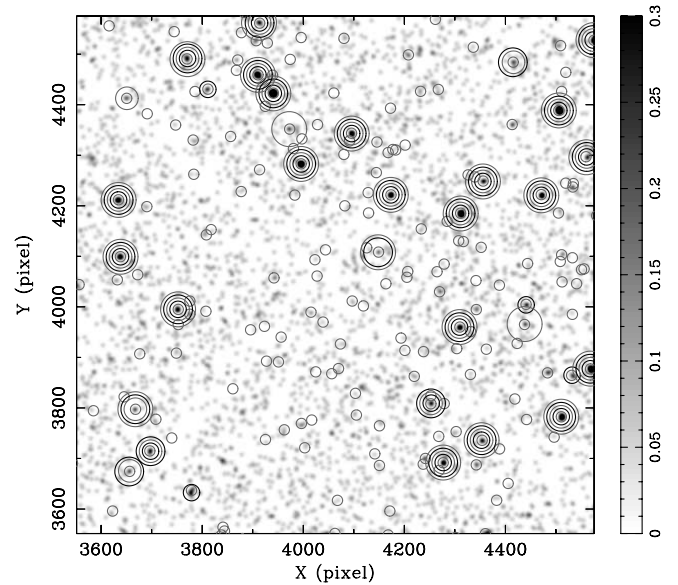


FIG. 11.—A 28.1 ks exposure from ObsID 3388 of the CDF-N. For this figure, the data have been smoothed. The smallest circles show the source locations from the 2 Ms deep catalog. The next three larger circles represent `lextrct` source finding using circular Gaussians, elliptical Gaussians, and PSFLIB. The largest circles represent sources found by the CIAO routine `wavdetect`. The undetected sources, i.e., the isolated small circles, appear to contain more counts than one expects from chance. This is correct in that the 157 sources not found by the `lextrct` circular Gaussian method contain 174 counts, whereas 50 would be expected from background alone. Of course, there are equally significant peaks that are not associated with real sources.

Figure 11 by the second smallest circles. If we lower the threshold, the brightest source found that is not in the 2 Ms catalog (i.e., a potential false positive) had a S/N of 1.89 and so could not be considered real. Although setting a S/N of 1.9 would result in six additional (faint) sources, we do not feel this is justified. It is worth noting that over this part of the image sources are photon-limited, and thus, there is no need for the additional requirement that sources be 5σ above background. Removing this limit resulted in no additional sources being detected.

A2.2. Elliptical Gaussian Model PSF

The second way that the PSF was modeled began by fitting the images in PSFLIB⁷ to elliptical Gaussians. PSFLIB contains a finite set of images representing the PSF at a series of off-axis distances and angles relative to the nominal aim point for different source energies. The tilt of the ellipse can be expressed as a simple function of the angle from the source to the aim point, where the angle is measured in a detector-based coordinate system. Although there is some change in this angle as you move off-axis, this change is ignored. The lengths of the major and minor axes were found at selected off-axis angles and then interpolated. For this method we did not inflate the size of the PSF model, and thus, S/N values were typically smaller than are seen with the circular Gaussian method. Thus, for a minimum S/N of 1.7 we found 27 sources, and again removing the requirement that sources be 5σ above background did not result in any additional sources being found. Using a σ value in the PSF model about 1.5 times larger increased the S/N to values similar to those found from the circular Gaussian method. Although the same total number of sources were found, the individual sources were not all the same. This method both found and missed four sources

⁷ See [ftp://cda.harvard.edu/pub/arcftp/caldb/acis-psflib-2.9.tar](http://cda.harvard.edu/pub/arcftp/caldb/acis-psflib-2.9.tar).

when compared to the circular Gaussian. All sources found were listed in the 2 Ms catalog.

A2.3. PSFLIB Model PSF

The third way that `lextrct` models the PSF is to extract the PSFLIB image that is closest to the position and then rotate the image to the correct roll angle. No interpolation between images is attempted, and in fact, to speed up this method, the array is not reloaded if the same PSFLIB image is used. This method gives only slight differences from the elliptical Gaussian function. Thus, to a $S/N = 1.7$ we found 27 sources, which are shown in Fig. 11 with the fourth smallest circles. Once again, lowering the minimum σ value above background resulted in no additional sources. Of these sources, 26 were also found by the elliptical Gaussian, whereas this method found and missed one each.

A2.4. Comparison to `wavdetect`

Finally, we used the CIAO-provided `wavdetect` tool with the default parameters. Effectively, `wavdetect` models the PSF with the Mexican hat function that is negative at certain radii. Both `lextrct` and `wavdetect` effectively have Gaussian cores, and therefore, both methods effectively give more weight to events grouped close to the center of the PSF. This represents an improvement over an earlier method called `cell detect`, which only considered the number of counts within a detection cell and not how they were grouped. The `wavdetect` tool found 25 sources in our sample field, and these positions are plotted in Fig. 11 with the largest circles.

A2.5. Full Field

We also searched the entire ACIS-I array for sources. For this search we binned the data into $0''.984$ (two detector) pixels. When we histogrammed the S/N distribution, both the Gaussian noise peak and the exponential tail were clearly detected. The data lay above the pure exponential for S/N values of 2.2 and lower. We selected 2.4 as our threshold. With this threshold we did find one source with a $S/N = 2.47$ that is not included in the 2 Ms catalog. Interestingly, the next two uncataloged sources (potential false positives) are at S/N values of 2.23 and 2.16, suggesting that the 2.47 value is unusually high for a noise peak. We note that one false detection in a field is considered acceptable.

A3. SUMMARY

Considering the union of all the source-finding methods considered for the field illustrated in Figure 11, 34 unique sources were found. Twenty-one sources were found by every method, and the remaining 13 sources were missed by at least one method. Of the 13 sources missed by one method, none was brighter than 10 detected counts. Likewise, no known source with an estimated flux of greater than 10 detected counts was missed by any method. Thus, we feel that all methods are fairly complete down to 10 detected events. At the center of the image, we can occasionally detect sources down to just four detected events. For a small number of counts, the precise position of these events in comparison to the template has an impact on the statistical significance. Thus, a source found with a S/N of 2.02 with one method could have a S/N of 1.95 with another method. If the threshold is set at 2.00, then one method would find the source and the second would miss it. In other words, the probability of detection depends on both the number of counts detected and their spatial distribution.

By plotting S/N versus detected counts C , we find that $S/N = 0.9\sqrt{C}$. For an ideal method and no background, the coefficient should be 1.0, close to the measured value. Using this relation, we find that a S/N of 2.4 corresponds to a detection threshold of about 7 counts. Thus, if there are 7 source counts in the image, there is about a 50% chance that the calculated S/N lies above the threshold value. Based on the scatter, some sources with only 5–6 counts will be detected, and most sources with 10 or more counts will be detected. This should not be confused with Poisson statistics that cause the number of detected counts to vary. After the counts are detected, there is an additional probability that the source will actually be detected by the method. Although some sources can be detected with only 4–5 counts, the efficiency for detection at this level is typically very low. Thus, the faintest detected source should not be used to determine the sensitivity of the detection method.

In summary, `lextrct` source-finding with the default circular Gaussian provides a reasonably complete source list down to 10 counts. Occasionally, sources as faint as 4 detected counts would be detected, but in no way should this be considered a sensitivity limit. A more reasonable sensitivity limit would be 7 counts, meaning that there is about a 50% chance of detecting a source at that level.

REFERENCES

- Alexander, D. M., et al. 2003, *AJ*, 126, 539
 Arnaud, K. 1996, in *ASP Conf. Ser. 101, Astronomical Data Analysis Software and Systems V*, ed. G. Jacoby & J. Barnes (San Francisco: ASP), 17
 Barger, A. J., et al. 2003, *AJ*, 126, 632
 de Blok, W. J. G., & Walter, F. 2000, *ApJ*, 537, L95
 Dickey, J. M., & Lockman, F. J. 1990, *ARA&A*, 28, 215
 D'Odorico, S., Dopita, M. A., & Benvenuti, P. 1980, *A&AS*, 40, 67
 Eskridge, P. B., & White, R. E., III. 1997, *AJ*, 114, 988
 Fabbiano, G., Kim, D.-W., & Trinchieri, G. 1992, *ApJS*, 80, 531
 Gallart, C., Aparicio, A., & Vilchez, J. M. 1996, *AJ*, 112, 1928
 Grimm, H.-J., Gilfanov, M., & Sunyaev, R. 2003, *MNRAS*, 339, 793
 Kong, A. K. H., Sjouwerman, L. O., & Williams, B. F. 2004, *AJ*, 128, 2783
 Markert, T. H., & Donahue, M. E. 1985, *ApJ*, 297, 564
 Monet, D. G., et al. 2003, *AJ*, 125, 984
 Peres, G., Orlando, S., Reale, F., Rosner, R., & Hudson, H. 2000, *ApJ*, 528, 537
 Pietrzyński, G., Gieren, W., Udalski, A., Bresolin, F., Kudritzki, R.-P., Soszyński, I., Szymański, M., & Kubiak, M. 2004, *AJ*, 128, 2815
 Prestwich, A. H., Irwin, J. A., Kilgard, R. E., Krauss, M. I., Zezas, A., Primini, F., Kaaret, P., & Boroson, B. 2003, *ApJ*, 595, 719
 Swartz, D. A., Ghosh, K. K., McCollough, M. L., Pannuti, T. G., Tennant, A. F., & Wu, K. 2003, *ApJS*, 144, 213
 Tennant, A. F., Wu, K., Ghosh, K. K., Kolodziejczak, J. J., & Swartz, D. A. 2001, *ApJ*, 549, L43
 van den Berg, S. 2000, *The Galaxies of the Local Group* (Cambridge: Cambridge Univ. Press)
 Weisskopf, M. C., Brinkman, B., Canizares, C., Garmire, G., Murray, S., & Van Speybroeck, L. P. 2002, *PASP*, 114, 1
 Wyder, T. K., Hodge, P. W., & Zucker, D. B. 2000, *PASP*, 112, 1162